

Cite this: *Energy Environ. Sci.*,  
2026, 19, 2367

# Microstructure of electrodeposited lithium and its evolution during cycling when using metal interlayers in “anode-free” solid-state batteries

Juri Becker,  †<sup>a</sup> Luca Schuster,  †<sup>a</sup> Sascha Kremer,<sup>a</sup> Till Fuchs  \*<sup>b</sup> and Jürgen Janek  \*<sup>a</sup>

“Reservoir-free” construction of solid-state batteries could circumvent the handling of reactive lithium metal foils and further increase the energy density. Metallic interlayers could play an important role in the homogenization of the electrodeposited lithium layer by increasing the coverage of the deposit and additionally reducing the size of the lithium grains. To date, the influence of different interlayers and the influence of stripping on the lithium microstructure is still unknown. This work analyzes the influence of gold, silver and bismuth interlayers on the microstructure of electrodeposited lithium layers using electron backscatter diffraction (EBSD) on cross-sections prepared by broad ion beam milling. In addition, partially stripped lithium layers and thus the influence of stripping on the lithium microstructure are analyzed using the mentioned interlayers. Our findings reveal that different interlayer materials result in different lithium microstructures. In addition, stripping also causes a significant change in the lithium microstructure, both in terms of grain size and grain orientation, gaining a deeper understanding of the lithium microstructure and its impact.

Received 27th November 2025,  
Accepted 3rd March 2026

DOI: 10.1039/d5ee07230a

rsc.li/ees

## Broader context

The development of safe and durable batteries with high energy density is a prerequisite for the wider use of renewable energies. Solid-state batteries address these demands, particularly through reservoir-free cell designs that eliminate pre-formed lithium metal electrodes by electrodepositing lithium only during the first charging cycle. While this approach simplifies manufacturing and maximizes energy density, controlling the lithium morphology during charging is critical to prevent capacity loss and cell failure. Currently, metallic interlayers, such as gold, silver, and bismuth, are widely used to improve lithium morphology. However, their impact on the resulting lithium microstructure, *i.e.*, grain size and orientation, remains largely unexplored. Moreover, the microstructural evolution of lithium during electrodisolution (discharge) is unknown. Understanding these phenomena is essential, as the microstructure affects the resulting electrochemical performance. Using electron backscatter diffraction on lithium layers electrodeposited in reservoir-free cells, this study demonstrates that metallic interlayers strongly influence the grain size and orientation of lithium. Furthermore, discharging is shown to alter both the grain size and orientation of lithium, too. These results highlight that interlayers not only affect morphology but also the microstructure of electrodeposited lithium, establishing microstructure-driven design principles for the development of advanced solid-state batteries.

## Introduction

Solid-state batteries (SSBs) can achieve higher energy and power densities compared to today's commercially available lithium-ion batteries by enabling the use of thin lithium metal electrodes (LMEs).<sup>1–3</sup> Lithium has a high theoretical capacity of

$q_{\text{th}} = 3860 \text{ mAh g}^{-1}$  and the lowest potential of  $-3.04 \text{ V}$  against the standard hydrogen electrode. Solid electrolytes (SEs) are intensively investigated, as they are often chemically and mechanically more stable against lithium metal and dendrite formation compared to liquid electrolytes.<sup>1</sup>

Despite a variety of advantages, the use of LMEs is hindered by the high reactivity of lithium, which leads to formation of passivation layers on its surface.<sup>4</sup> Minimizing the interfacial resistance in combination with SEs originating from these layers requires costly storage and manufacturing in an inert atmosphere.<sup>5</sup> Alternative solutions, such as mechanically removing passivation layers or applying high temperature and pressure during cell preparation, also increase costs, making them less desirable.<sup>6,7</sup>

<sup>a</sup> Institute of Physical Chemistry and Center for Materials Research (ZfM), Justus-Liebig-University Giessen, Heinrich-Buff-Ring 17, D-35392 Giessen, Germany.

E-mail: juergen.janek@pc.jlug.de

<sup>b</sup> Institute of Experimental Physics I and Center for Materials Research (ZfM), Justus-Liebig-University Giessen, Heinrich-Buff-Ring 16, D-35392 Giessen, Germany. E-mail: till.fuchs@uni-giessen.de

† Equal contribution.



To address these challenges, reservoir-free concepts (RFCs), often referred to in literature as “anode-free” cell concepts are being explored.<sup>8–10</sup> These cells consist of a lithiated positive electrode material, a SE, and current collectors (CCs). No lithium metal is present on the negative electrode side upon assembly. During charging, lithium is electrodeposited at the CC|SE interface on the negative electrode side. This concept eliminates the need to handle lithium metal, thereby simplifies fabrication, and increases energy density further. Additionally, electrodeposition using single-ion conducting SEs produces chemically pure lithium layers, enhancing discharge capacity.<sup>11,12</sup>

However, RFCs suffer from morphology-driven cell failure during cycling. Inhomogeneous lithium deposition often leads to dendrite formation and poor CC coverage.<sup>13–15</sup> Lithium stripping can cause pore formation and contact loss,<sup>16–18</sup> as SEs cannot compensate for volume changes of the electrodes. A promising and widely-investigated strategy to mitigate these issues is the use of interlayers at the CC|SE interface.<sup>10,19–25</sup> Alloying elements are intensively studied to homogenize the lithium morphology during plating and to mitigate pore formation during stripping.<sup>10,19,20,23,24,26–28</sup> Gold and silver, in particular, are being investigated because they can increase lithium nucleation density and thereby prevent dendrite formation during lithium electrodeposition when using sulfide SE materials such as  $\text{Li}_6\text{PS}_5\text{Cl}$  (LPSCl).<sup>10,20,29</sup> Furthermore, they can easily be prepared as chemically pure thin films. Additionally, alloy materials such as bismuth are also being investigated as cost-effective alternatives. In addition, the high Young's modulus of  $\text{Li}_3\text{Bi}$  alloys is expected to prevent dendrite formation.<sup>27,30</sup> Beyond these effects, interlayers were recently linked to changes in the microstructure of electrodeposited lithium metal, decreasing its grain size and changing from a columnar microstructure to a less ordered one.<sup>31</sup> Control of the microstructure of lithium is considered a crucial parameter to improve cycling stability of LMEs.<sup>32–34</sup>

A key parameter of microstructure control is the grain size. Grain boundary (GB) density of electrodeposited lithium should be high, as GBs are predicted to act as fast diffusion pathways potentially preventing void formation during stripping.<sup>35</sup> However, for practically relevant lithium layer thicknesses of  $\sim 25 \mu\text{m}$  of lithium (corresponding to  $\sim 5 \text{mAh cm}^{-2}$ ), the deposited lithium typically exhibits large lateral grain sizes in the order of  $\sim 100 \mu\text{m}$ , whereas significantly smaller grains with a size of  $\sim 1 \mu\text{m}$  would be more favorable.<sup>33–35</sup> The introduction of interlayers provides a potential route to tuning this microstructure during electrodeposition.<sup>31,36</sup>

Prior studies have primarily focused on the lithium microstructure after initial electrodeposition.<sup>31,33,34</sup> However, its evolution during stripping is of equal importance, as changes in the lithium microstructure, such as preferential orientation, can directly affect stripping parameters such as available capacity and critical current densities. Recently, single-crystalline lithium films were used to show that lithium orientation influences the electrochemical properties of

lithium electrodes.<sup>37</sup> Furthermore, it was previously shown that the lithium microstructure changes during deposition.<sup>33,34</sup> Conversely, stripping could also lead to microstructural changes and thus changes in the stripping properties during operation. Understanding these changes is essential for improving cycling stability.

To address this, we analyzed lithium layers electrodeposited onto various interlayers using Ti|interlayer|LPSCl|Li|Ti model-type RFCs, selecting gold, silver and bismuth as interlayer materials. Titanium was used as CC due to its chemical stability against LPSCl and lithium.<sup>38</sup> To gain deeper insight into the microstructural effects of these interlayers, wide cross-sections of the electrodeposited lithium layers were prepared and analyzed using electron backscatter diffraction (EBSD), revealing distinct mechanisms by which different interlayer elements influence the lithium microstructure. Additionally, lithium layers were analyzed after partial stripping of the electrodeposited layer to examine the effects of subsequent lithium stripping on the microstructure. A significant change in the preferential orientation of lithium was observed, especially in cells using pristine metal foils as CCs. Furthermore, the microstructural evolution of the electrodeposited lithium layers after multiple cycles was investigated. The results show that both interlayers as well as (repeated) stripping and plating cause notable changes in the lithium microstructure. Depending on the phase diagram of the lithium–interlayer system and the thickness of the interlayer, alloying interlayers can either completely or partially dissolve in deposited lithium, form intermetallic phases or remain virtually unchanged. We consider the resulting phenomena as a specific case of “electrometallurgy” in batteries.

## Experimental

### Cell preparation

Cell preparation was performed in a glove box (LABmaster pro, MBraun, Germany) under argon inert gas with residual water and oxygen contaminations  $< 1 \text{ppm}$ , and nitrogen contaminations  $< 10 \text{ppm}$ . Commercial LPSCl (POSCO Chemical Co, Korea) with a particle size of  $5 \mu\text{m}$  was used as SE for the construction of all cells. The counter electrode (CE) was prepared by cutting lithium with a purity of 99.8% (MaTecK Material-Technologie & Kristalle GmbH, Jülich, Germany) from a rod. The passivation layer was then removed mechanically, and the material was pressed by hand between two pouch foils to form a foil with a thickness of approximately  $100 \mu\text{m}$ . Finally, circular electrodes were punched out from the foil ( $d_{\text{CE}} = 9 \text{mm}$ ). A titanium foil (Goodfellow Cambridge Ltd, UK, 99.99% purity) with a thickness of  $15 \mu\text{m}$  was used as the working electrode ( $d_{\text{WE}} = 10 \text{mm}$ ). In instances where an interlayer was employed at the working electrode side, a thin film of gold, silver, or bismuth was deposited onto the titanium foil by using an in-house physical vapor deposition (PVD) chamber. For this, titanium foils were clamped inside a mask and a  $160 \text{nm}$  thick layer of the desired interlayer material was



deposited onto the titanium with a deposition rate between 0.2–0.3 nm s<sup>-1</sup>. Cells were assembled using self-made press cell casings made out of brass with a polyether etherketone (PEEK) mantle of 10 mm diameter. The working electrode was placed on one of the steel stamps inside the press cell. Subsequently, 90 mg of LPSCl powder was filled in using a funnel. Both stamps were fixed and sealed using nitrile butadiene rubber (NBR) rings. The powder was then compacted uniaxially once for three minutes at a pressure of 380 MPa. The stamp was then removed on the CE side, a hand-pressed lithium foil was applied with a titanium foil on top and the stamp was reinserted. Finally, the finished press cell was clamped in an aluminum frame and a stack pressure of 15 MPa was applied. Before starting the electrochemical characterization, the cell was left to rest for at least five hours.

### Electrochemical characterization

All electrochemical experiments were carried out using potentiostats from BioLogic (VMP3 or VMP300, BioLogic, France). Before characterization, all cells were equilibrated. During the resting period, potentiostatic electrochemical impedance spectroscopy (PEIS) was carried out between 7 MHz and 100 mHz at an amplitude of 10 mV. Subsequently, lithium was deposited using chronopotentiometry (CP). For the deposition of 7.5 mAh cm<sup>-2</sup> of lithium with and without interlayers, and for the cycling experiments where 4.5 mAh cm<sup>-2</sup> of lithium were electrodeposited and stripped for 10 cycles, a current density of 150 μA cm<sup>-2</sup> was used. A current density of 100 μA cm<sup>-2</sup> was used for the deposition of 10 mAh cm<sup>-2</sup> and subsequent stripping of 5 mAh cm<sup>-2</sup> of lithium. To assess the voltage profiles of various alloy phases during the initial stage of lithium electrodeposition onto an interlayer, a lithium deposition *via* CP with reduced current density was conducted. In this case, a current density of 3 μA cm<sup>-2</sup> was applied until the maximum theoretical lithium areal charge for full lithiation of the interlayer was achieved, followed by lithium deposition. After successful electrodeposition, cells were disassembled for further analysis within the glovebox.

### Cryogenic ion-milling

Cross-sections of electrodeposited lithium with and without interlayers were prepared *via* ion beam milling using a Leica EM TIC 3X (Leica Microsystems, Germany) at temperatures below -100 °C. The working electrodes of the samples were detached from the cell stack and transferred into the Leica EM TIC 3X using an inert transfer system (Leica VCT500, Leica Microsystems, Germany). The milling was conducted at an accelerating voltage of 6 kV and an Ar<sup>+</sup> ion current of 2.2 mA.

### Electron backscatter diffraction (EBSD)

To minimize passivation reactions, the polished cross-sections were immediately transferred to the SEM using the Leica VCT500. The lithium layer was then analyzed with a symmetry 3 EBSD detector (Oxford Instruments, England) at an accelerating voltage of 10 kV and a probe current of approximately 12 nA. All measurements were conducted at a working distance

of roughly 12.5 mm and a tilt of 70°. If the Kikuchi pattern quality was found to be insufficient, the accelerating voltage was increased to either 15 kV or 20 kV.

### Data processing and analysis

Post-processing of the acquired measurement data was carried out using the AZtec Crystal software (Oxford Instruments, England) with the implemented MapSweeper tool. Indexing was done using a Hough algorithm with a resolution of 60 and 11 bands considering the cubic Li (*Im*3̄*m*) phase. To refine the measured EBSD patterns of lithium and eliminate artifacts like pseudo-symmetries within grains, dynamical template matching, refinement sweeps, and repair sweeps were performed using a master simulation of EBSD patterns.

### Grain growth simulations

Grain growth was simulated using a Monte Carlo Potts model, as frequently applied to simulate normal grain growth, the influence of texture, recrystallization, particle pinning, and many other phenomena.<sup>34,39–51</sup> In our implementation, the lithium metal microstructure is discretized onto a cubic lattice, with each lattice site *i*, referred to as a Monte Carlo unit (MCU), assigned a grain orientation  $\vartheta_i$ , represented as an integer between 1 and 240. Grain boundaries are implicitly defined at interfaces between neighboring MCUs *i* and *j* with differing orientations ( $\vartheta_i \neq \vartheta_j$ ). The total energy of the system  $E_{\text{tot}}$  is computed as:

$$E_{\text{tot}} = \frac{1}{2} \sum_{i=1}^N \sum_{j=1}^{\text{nn}=26} \gamma_{i,j}^{\text{gb}} (1 - \delta(\vartheta_i, \vartheta_j)),$$

where  $\gamma_{i,j}^{\text{gb}}$  is the energy of a unit of boundary between MCU *i* and one of its 26 nearest-neighbor (nn) MCUs *j* (6 first nearest, 12 second nearest, and 8 third nearest-neighbors). *N* is the number of lattice sites, and  $\delta(\vartheta_i, \vartheta_j)$  is the Kronecker delta, yielding 1 if  $\vartheta_i = \vartheta_j$  and 0 otherwise. In practice the grain boundary energy, thus  $\gamma_{i,j}^{\text{gb}}$ , is a function of the misorientation angle of adjacent grains.<sup>41,49,52</sup> Anyhow, the orientation dependence of  $\gamma_{i,j}^{\text{gb}}$  was neglected ( $\gamma_{i,j}^{\text{gb}} = \gamma_{\text{const}}^{\text{gb}}$ ), resulting in curvature driven grain growth.<sup>39,46</sup> Grain growth proceeds *via* a Monte Carlo algorithm: a randomly selected MCU attempts to adopt the orientation of one of its 26 neighbors. The new configuration is accepted with a probability *P* based on the energy change  $\Delta E_{\text{tot}}$  between the new and the old state:

$$P = \begin{cases} 1 & \text{if } \Delta E_{\text{tot}} \leq 0 \\ \exp(-\Delta E_{\text{tot}}/T_s) & \text{if } \Delta E_{\text{tot}} > 0, \end{cases}$$

Here,  $T_s$  is the simulation temperature, which is a technical parameter that determines the acceptance probability for state changes that increase the total energy of the system.<sup>52</sup> We set  $T_s = \gamma_{\text{const}}^{\text{gb}}$  throughout all simulations. A full Monte Carlo step (MCS) consists of *N* such reorientation attempts. For a domain size of 30 · 250 · 250 MCUs, this corresponds to  $\approx 2 \cdot 10^6$  updates per MCS.

To investigate the influence of the lithium film thickness, we followed an approach used by Zöllner *et al.*:<sup>41–43</sup> free surfaces



were introduced as boundary conditions at the top and bottom surfaces (parallel to the CC|SE interface), such that MCUs on the surface have only 17 instead of 26 neighbors. As for all other simulations, periodic boundary conditions were used in the other two directions. Similar to our previous work,<sup>34</sup> the influence of the SE and CC interfaces was considered by attaching static polycrystalline layers to the lithium domain. These layers act as domains with fixed orientations and do not evolve during the simulation. The interfacial energy  $\gamma_{ij}^{\text{int}}$  between a lithium MCU  $i$  and an adjacent fixed MCU  $j$  is treated analogously to  $\gamma_{ij}^{\text{gb}}$ , yielding  $\gamma_{\text{const}}^{\text{gb}}$  if  $\vartheta_i \neq \vartheta_j$  and 0 otherwise. Hence, these fixed layers may be understood as thin lithium layers on top of the SE/CC that are forced into distinct low-energy orientations with respect to the SE/CC grains or SE/CC grain itself.

To study the effect of secondary-phase particles, we followed another common approach from the literature<sup>51</sup> that is similar to the one used to incorporate the SE/CC influence: immobile spherical inclusions with a diameter of 3 MCUs were introduced. These MCUs were assigned a unique, fixed orientation/integer (250), which cannot be adopted by the lithium MCUs. This enforces a constant interface energy  $\gamma_{ij}^{\text{int}} = \gamma_{\text{const}}^{\text{gb}}$  at the particle surface. The same strategy was used to explore the influence of interfacial roughness by placing two roughened layers (also with fixed orientation 250) adjacent to the lithium film.

To simulate large 3D structures within a feasible runtime, we adopted an approach discussed in more detail by Wright *et al.*<sup>48</sup> that enables efficient parallelization of some computation steps on a GPU. For parallelization, the lattice is partitioned into 8 sublattices with non-interacting MCUs, that do not share neighbors. In each update step, one sublattice is randomly selected, and all its MCUs are updated in parallel. Repeating this 8 times completes one MCS. All simulations were carried out in Python. Computationally expensive tensor operations were implemented using Pytorch.<sup>53</sup> In Fig. S1, the simulation approach and boundary conditions are schematically shown.

It is important to note that the Potts model used operates in arbitrary units, neglects the influence of electrodeposition kinetics, and does not provide direct access to physical time, length, or energy scales. Additionally, the Potts model relies on simplified, often arbitrary update rules and energy definitions and the simulated grain microstructure is influenced by the underlying simulation lattice (lattice pinning). Consequently, the results should be interpreted as qualitative insights into the evolution of curvature driven grown grain structures under special geometric and interfacial constraints (*e.g.*, thin-film geometries, pinning, substrate interaction, interface roughness), rather than quantitative predictions of experimental grain growth kinetics.

## Results and discussion

### Influence of interlayers on the resulting lithium microstructure

To study the influence of interlayers on the lithium electrodeposition and resulting microstructure, a Ti|interlayer|LPSCl|Li|Ti model system was used, as schematically depicted in Fig. 1a.

Additionally, as reference, cells without interlayer, *i.e.*, Ti|LPSCl|Li|Ti were also analyzed. The voltage profiles for lithium deposition using gold, silver and bismuth as interlayer as well as the titanium reference are shown in Fig. 1b. In all cases, an areal charge of 7.5 mAh cm<sup>-2</sup> (nominally 37.5 μm) was deposited at a current density of 150 μA cm<sup>-2</sup>. A microstructural analysis of the electrodeposited lithium layers was conducted using EBSD on prepared cross-sections. Representative regions from the large area cross-sections are given in Fig. 1c.

Similar to steel, no additional lithium loss could be seen for titanium in CTTA experiments (see Fig. S2). Titanium<sup>38</sup> has the advantage that, unlike steel, it is a chemically pure metal. For the titanium foil without interlayer, the voltage profile first passes through a minimum, which is associated with lithium nucleation.<sup>8</sup> Once the voltage stabilizes around 10 mV, agreeing with the IR drop of the cell, the previously formed lithium nuclei grow in size and the analyzed grains in Fig. 1b form.

Gold has already been established as a suitable interlayer material, due to its chemical stability and its ability to form a stable Li<sub>x</sub>Au alloy during lithiation, which promotes uniform lithium electrodeposition.<sup>10,13,20,31,54</sup> The voltage profile when electrodepositing lithium on a gold layer shows only two plateaus at 260 mV and 120 mV, despite passing through more phases in the phase diagram. As the potentials of the other phases are very close to each other, the transitions might be masked by the kinetics and the corresponding overpotentials. Furthermore, the relatively high current density of 150 μA cm<sup>-2</sup> could lead to a kinetic inhibition of some phases, which is why they are not observed here, despite being predicted by the phase diagram. In addition, some of the lithium-gold alloy phases appear to be unstable up to the δ-phase.<sup>26,55</sup> After reaching a negative potential, lithium nucleates, as indicated by a small minimum in the voltage profile.<sup>31</sup> To gain further insight in the lithiation process, the current density was decreased to 3 μA cm<sup>-2</sup> in a second cell. Furthermore, coulometric titration (CT) experiments coupled with an electrochemical impedance analysis were conducted on a third cell. Here, an additional plateau at 20 mV appears (see Fig. S3 and S4 and Note S1), corresponding to the Li<sub>3</sub>Au|Li<sub>15</sub>Au<sub>4</sub> two-phase region, underlining the kinetic inhibition of certain phases. At this point, we like to highlight that alloys investigated in binary phase diagrams are in most cases produced from a melt of the two constituent metals, while alloy formation at room temperature has often not been systematically investigated and is frequently based on data extrapolated from high temperatures. Therefore, their reliability at room temperature is uncertain and must be considered when interpreting phase stability and alloy formation.

Silver was also used as an interlayer material, due to its chemical stability and the formation of a stable Li<sub>x</sub>Ag alloy.<sup>10,19,28,31,54</sup> This and faster lithium diffusion was shown to lead to a uniform lithium deposition and an increased cycle life of RFCs. The voltage profile when electrodepositing lithium on a silver layer, shows virtually no voltage plateaus, even if expected from the phase diagram.<sup>31,56</sup> Here, again, kinetic limitations are likely the reason, as additional voltage plateaus





**Fig. 1** Electrodeposition of lithium using (a) different interlayer materials. (b) Voltage profiles of the respective cell systems ( $T = 25\text{ }^{\circ}\text{C}$ ,  $j = 150\text{ }\mu\text{A cm}^{-2}$ ). As schematically depicted, titanium was used as reference (top row) and gold (2nd row), silver (3rd row) and bismuth (4th row) were used as interlayer materials. (c) Microstructure of the electrodeposited lithium layers using the different interlayer materials. The IPF maps are given parallel to the  $y$ -direction as indicated above. The shown scalebar represents  $50\text{ }\mu\text{m}$  in all cases. (d) IPFs of the analyzed cross-sections showing the distribution of the orientation of all analyzed grains. The IPFs are given parallel to the  $y$ -direction. Please note that the IPFs were created based on the entire analyzed cross-section, which is shown in the SI.

can be resolved when decreasing the current density to  $3\text{ }\mu\text{A cm}^{-2}$  as well as in the CT experiments (see Fig. S3 and S4). Interestingly, the voltage drops directly below  $0\text{ V}$  without an additional (nucleation) overpotential.

Lastly, bismuth was chosen as interlayer material due to its affordability, and electrochemical activity, forming a  $\text{Li}_x\text{Bi}$  alloy during lithiation with improved lithium diffusion.<sup>57,58</sup> It could therefore be a cost-effective alternative to more established alloying interlayer materials such as gold or silver. The voltage profile when electrodepositing lithium on a bismuth layer, shows two plateaus at  $800\text{ mV}$  and  $760\text{ mV}$  before the potential drops below  $0\text{ V}$ . These two voltage plateaus correspond to the two 2-phase regions  $\text{Bi|LiBi}$  and  $\text{LiBi|Li}_3\text{Bi}$  in the  $\text{Li-Bi}$  phase diagram.<sup>56</sup> The experiment was repeated with a lower current density of  $3\text{ }\mu\text{A cm}^{-2}$  and *via* CT. The potential profile can be seen in Fig. S3 and S4. After dropping below  $0\text{ V}$ , electrodeposition of lithium metal takes place after passing through a small nucleation minimum.

Microstructural analysis of the electrodeposited lithium layer on the pristine titanium foil reveals large columnar grains with almost all grain boundaries being perpendicular to the SE interface with some truncated grains forming at the  $\text{Li|LPSCl}$  interface. This microstructure is in good agreement with previously studied lithium layers electrodeposited on various  $\text{CC|SE}$  interfaces.<sup>33,34</sup> As the grain width is determined by the electrodeposited lithium layer thickness,<sup>34</sup> the large grain size

in this case, suggests similar trends for lithium layers electrodeposited at  $\text{Ti|LPSCl}$  interfaces. Another similarity is that the grown lithium grains do not appear to exhibit a pronounced preferential orientation, as can be seen in the inverse pole figures in Fig. 1d. However, the lithium microstructure on titanium foil appears to be slightly more distorted locally than on *e.g.* steel foil previously used.<sup>34</sup> This could be due to the different microstructure and larger average grain sizes of the titanium foil ( $\bar{A}_{\text{grain}} \approx 150\text{ }\mu\text{m}^2$ , see Fig. S5) compared to steel foil ( $\bar{A}_{\text{grain}} \approx 0.8\text{ }\mu\text{m}^2$ ).<sup>34</sup> A detailed discussion of the influence of the substrate on the resulting lithium microstructure will follow below. For the inverse pole figures in parallel to the  $x$ - and  $z$ -axis, the reader is referred to Fig. S6 along with the full cross-sections displayed in Fig. S7.

The microstructural analysis of the lithium layer electrodeposited on a gold interlayer reveals a mix of thin columnar grains, multiple smaller grains at the  $\text{Ti|Li}$  interface and stacked grains as can be seen from the excerpt shown as well as the full cross-section in Fig. S8. While some columnar grains can be seen, the lithium microstructure deviates significantly from a mere columnar form, exhibiting more substantial deviations than what is observed on bare titanium CCs or on steel and copper CCs used in recent studies.<sup>33,34</sup> These results are in line with those of Haslam and Fuchs *et al.* who found a similar microstructure of lithium electrochemically deposited at  $\text{Cu|LLZO}$  interfaces with a gold interlayer,<sup>31</sup> despite the



different CC and SE. Thus, we conclude that the microstructure is influenced primarily by the interlayer and is apparently less dependent of CC and SE. Interestingly, making use of the better statistics due to large cross-sections, a preferred orientation in the  $\langle 101 \rangle$  directions parallel to the  $y$ -axis is indicated in the inverse pole figure in Fig. 1d for the gold interlayer. For the inverse pole figures in parallel to the  $x$ - and  $z$ -axis, the reader is referred to Fig. S6. The full cross-section can be seen in Fig. S8.

For a silver interlayer, the microstructural analysis of the lithium layer reveals a mostly columnar structure, but with much thinner grains compared to the lithium grains electrodeposited without an interlayer. These differences in the aspect ratio, *i.e.*, the ratio of grain height to grain width, are summarized for all electrodeposited lithium layers in Fig. S9. This was already indicated in a previous study<sup>31</sup> and is now proven here using the wide cross-sections. Additionally, the statistical analysis reveals that lithium grains exhibit a preferred growth direction when electrodeposited on a silver interlayer. In contrast to gold, the  $\langle 111 \rangle$  direction parallel to the  $y$ -axis seems to be predominant in the case of silver as can be seen from Fig. 1d. For the inverse pole figures in parallel to the  $x$ - and  $z$ -axis, the reader is referred to Fig. S6. The full cross-section can be seen in Fig. S10.

Lastly, when using bismuth as interlayer, a columnar lithium microstructure can be found, similarly to the pristine titanium foil and the silver interlayer. However, unlike when other interlayer materials are used, the lithium grains are significantly larger, with a width even larger compared to that of the lithium layer electrodeposited on pristine titanium foil. The lithium grains show a preferred orientation in the  $\langle 101 \rangle$  and  $\langle 111 \rangle$  direction parallel to the  $y$ -axis as can be seen from the

inverse pole figure in Fig. 1d. Interestingly, one grain stands out, with a width of  $811 \mu\text{m}$  (compare Fig. S11). The possible cause of its origin is discussed later in this chapter.

One important benefit of the wide cross-sections prepared *via* ion beam milling in this work, is the possibility of quantitative comparison of the lithium microstructures in each case. Therefore, the whole cross-sections spanning several millimeters (see Fig. S7, S8, S10 and S11) of the lithium layers electrodeposited with and without interlayer were analyzed in terms of their layer height and grain width. The results are summarized in a box plot in Fig. 2a. In addition, energy dispersive X-ray spectroscopy (EDS) measurements were carried out in the case of the bismuth and silver interlayers to obtain information on the distribution of the interlayer materials. For gold, an EBSD measurement was performed on particles found within the electrodeposited lithium layer. The results are shown in Fig. 2b–d.

As shown in the upper part of Fig. 2a, the layer thickness deviates between the measured samples, even though the same areal charge of  $7.5 \text{ mAh cm}^{-2}$  was electrodeposited in all cases. This is due to changes in the coverage of the CCs used, as can be seen in Fig. S12. While there are still pristine areas for titanium and bismuth, the coverage in the case of gold and silver is close to 100%. This increase in coverage for gold and silver interlayers aligns well with recent studies on interlayers,<sup>10,13,31</sup> and leads to a reduced layer height compared to lithium plated at pristine CC metal foils.

Notably, the deposited lithium on a bare titanium CC exhibits the highest layer thickness, corresponding to the lowest degree of coverage. This could be attributed to the crystallographic mismatch between titanium (hexagonal) and lithium



**Fig. 2** Summary of the results from all analyzed lithium layers electrodeposited using different interlayers. (a) The average lithium layer thickness is shown in the upper part of the graph. The calculated (expected mean) height for  $7.5 \text{ mAh cm}^{-2}$  of  $37.5 \mu\text{m}$  is depicted with a dotted line. The grain width of the analyzed lithium grains is depicted in the box plot underneath. Here, 18 grains were analyzed in the case of electrodeposition on a pristine titanium foil, 11 for the bismuth interlayer, 64 for the gold interlayer and 70 for the silver interlayer, respectively. The average is marked with a triangle inside each box. Outliers (interquartile range factor = 1.5) are marked with points colored in the same way as the respective box. (b) EBSD analysis of the lithium layer electrodeposited using a gold interlayer (top: SEM image). (c) EDS analysis of a lithium layer electrodeposited using a silver interlayer (top: SEM image). (d) EDS analysis of the lithium layer electrodeposited using a bismuth interlayer (top: SEM image).



(cubic),<sup>59</sup> which may inhibit widespread nucleation during the initial stages of deposition. The average grain width in the case of the pristine titanium foil is with 136  $\mu\text{m}$  roughly twice as high as the layer height. This is also reflected in the aspect ratio of the grains, which is shown in Fig. S9 and is approximately 0.5 (ratio of height to width). This is in good agreement with previous results on electrodeposited lithium layers at a steel|Li<sub>6</sub>PS<sub>5</sub>Cl interface and indicates a curvature driven normal grain growth, as postulated by C. V. Thompson.<sup>34,60</sup>

In the case of the gold interlayer, the average grain width decreases to 30  $\mu\text{m}$  and is therefore significantly lower compared to the pristine titanium foil. At this point we would like to note that the layer thickness was shown to also influence the resulting grain width.<sup>34</sup> As the lithium layer electrodeposited with an gold interlayer is thinner compared to the one electrodeposited on a pristine titanium foil, this might further increase the difference in grain width between the two samples. However, the 4-fold decrease in grain width cannot solely be attributed to changes in the layer thickness. This is supported by the changed grain distribution and the higher aspect ratio of  $\approx 1.3$ .

In the case of the silver interlayer, the average grain width also decreases significantly to 30  $\mu\text{m}$ . As in the case of gold, the thickness of the lithium layer deposited on the silver interlayer is significantly lower than the layer thickness on the bare titanium foil, which highlights the higher CC coverage during the deposition when using gold and silver as interlayer materials. Interestingly, the average grain width with silver interlayer is close to the one with gold interlayer. Since both lithium layers show also approximately the same thickness, this could indicate that the layer thickness effect mentioned above is also present when using interlayers. However, as with gold, the reduced grain size compared to the lithium layer deposited on pure titanium cannot be attributed solely to a thickness effect, but an additional influence of the silver interlayer is evident, changing the grain distribution and increasing the aspect ratio to  $\approx 1.3$ .

Interestingly, the layer height of lithium deposited on a bismuth interlayer is only slightly lower than that of lithium deposited on titanium. It might be expected that the interlayer would promote lithium nucleation and lead to a higher degree of coverage, as is the case for gold and silver. However, this is not observed for bismuth. Also, in the case of the bismuth interlayer, the average grain width is with 170  $\mu\text{m}$  even higher as in the pristine titanium case, even though the layer thickness is slightly lower. The large grain mentioned above, is marked as the only outlier with a width of 811  $\mu\text{m}$ . The aspect ratio of the bismuth sample, at  $\approx 0.6$ , is also very close to the value for the bare titanium foil.

In general, it could be shown that the microstructure of electrochemically deposited lithium is modified with the help of interlayers. Bismuth tends to increase the size of the lithium grains present, while silver and gold lead to a significant reduction in the grain size. The reduced grain size could improve the stripping behavior of the electrode, as is shown by simulation results.<sup>35</sup> This improvement is attributed to the

higher density of grain boundaries, which serve as fast diffusion paths for lithium atoms. According to the simulations, grain sizes below 1  $\mu\text{m}$  are required to achieve current densities exceeding 1  $\text{mA cm}^{-2}$ .<sup>35</sup> To gain more insight into the underlying mechanisms of the different alloying materials, the prepared cross-sections were further analyzed using EDS and EBSD. These analyses provide information about the position of the interlayers and their chemical composition across the interface, revealing that all three interlayer materials are located at different positions/regions within the cross-section. For gold, small clusters were detected predominantly near the Ti|Li interface in Fig. 2b, originating from the evaporated gold interlayer. EBSD revealed Kikuchi patterns corresponding to the Li<sub>15</sub>Au<sub>4</sub> crystal structure. Although not visible in the voltage profile during electrodeposition, the alloy appears to form over time, indicating kinetic limitations during electrodeposition. These dispersed Li<sub>15</sub>Au<sub>4</sub> particles likely affect lithium grain growth through a mechanism similar to Zener pinning: grain boundaries encountering these clusters experience drag forces that slow down their migration and hinder further grain coarsening.<sup>61</sup>

In contrast, EDS analysis of lithium deposited on a silver interlayer in Fig. 2c shows a homogeneous silver distribution within the lithium layer. According to the Ag–Li phase diagram, silver can dissolve into lithium up to about 1 at% at room temperature.<sup>22,62</sup> Given the initial 160 nm thickness of the silver layer, its complete dissolution would occur beyond an areal charge of approximately 4.2  $\text{mAh cm}^{-2}$  of lithium, which is less than the total amount of deposited lithium here. Therefore, a homogeneous solid solution of silver in lithium is expected. As silver is dissolved within the lithium lattice, the high density of grain boundaries may result from altered mechanical properties rather than Zener pinning. The dissolved silver could induce lattice strain throughout the lithium layer, modifying its surficial energy and impeding grain growth without silver accumulating at the Ti|Li interface. This energy change is expected, as lithium with 1 at% silver should have a slightly lower melting temperature than pure lithium.<sup>31,62</sup> To analyze a possible change in crystal structure, a Li(Ag) solid solution with 0.7 at% silver in lithium was produced from a melt and examined using X-ray diffraction (XRD). As can be seen in Fig. S13 and Note S2, consistent with the literature,<sup>62</sup> a decrease in the lattice constants of the lithium lattice by 0.21% and thus a lattice contraction is detected. Please note that the sample examined by XRD was produced from melt and not by electrodeposition; nevertheless, the results qualitatively show the effect of dissolved silver in a lithium host lattice.

In case of bismuth, a bismuth layer is found at the LPSCl interface in Fig. 2d, suggesting that lithium begins depositing behind the interlayer only after alloy formation is complete. This in turn suggests that lithium must pass through the Li<sub>3</sub>Bi layer before accumulating at the Li<sub>3</sub>Bi|Ti interface, and that bismuth probably has a low diffusion coefficient in lithium. This finding may help explain the low coverage found in Fig. 2a and Fig. S12: despite the presence of bismuth, lithium deposition occurs in contact with titanium. Since bismuth does not



dissolve into lithium, the deposited lithium forms a pure layer without remnants of the bismuth interlayer. However, unlike the deposition of lithium on a bare titanium CC, the presence of the bismuth-rich interlayer on the LPSCI prevents interaction of the lithium with the SE, which, as previously found, affects the resulting lithium microstructure.<sup>34</sup> It is noteworthy that separation of the two reactive species, *i.e.*, lithium and LPSCI, also influences SEI formation.<sup>56</sup>

### Simulations of factors influencing lithium microstructure

Building on our experimental observation that different interlayers result in different lithium microstructures, we use simulations to gain a qualitative understanding of how microstructures are influenced under varying boundary conditions in the thin-film geometry. Since various influencing factors can always occur simultaneously in the experiment, we apply a three-dimensional Monte Carlo Potts model to separate the effects of layer thickness, particle fraction, substrate grain size, and substrate roughness. In these simulations, deposition kinetics are neglected. Instead, a film is deposited instantaneously to a certain thickness and its microstructural evolution is then observed over time. The results are summarized in Fig. 3.

Fig. 3a investigates the influence of the layer thickness on the resulting lithium microstructure. As already visible from the 3D microstructures and the 2D cross-sections underneath, the average grain width increases when increasing the layer thickness from 10 Monte Carlo units (MCU) to 30 MCU. The grain height evolution further reveals that all layers develop columnar structures during the simulation, as reflected by the fact that the average grain height approaches and eventually equals the respective layer thickness (10, 20, and 30 MCU). A distinct change in the slope of the grain width growth with time occurs once the grain height matches the layer thickness. This is attributed to a reduction in curvature-driven grain growth along the height direction: once grains reach the full height,

once grains reach the full height,



Fig. 3 Simulation results of lithium microstructure evolution under different conditions: (a) effect of lithium layer thickness, (b) secondary particle content and (c) substrate grain size. Each panel shows two 3D microstructures along with two 2D cross-sections underneath. On the right, the evolution of the average grain width ( $w_{Li}$ ) and height ( $h_{Li}$ ) versus simulation time in Monte Carlo steps (MCS) is shown.



further growth in that dimension no longer contributes to energy minimization. Consequently, growth continues only in-plane, driven by curvature reduction in that direction, resulting in a slower overall growth rate. Although grain growth slows down, it does not come to a complete stop in 3D. With sufficient simulation time and without other interactions, the system would ultimately develop into a single grain, which is a key difference from previous 2D simulations.<sup>34</sup> For the following simulations of the other influencing factors, the layer thickness is set to 20 MCU.

Fig. 3b shows the effect of secondary particles, mimicking the role of alloy inclusions in the experiment or other secondary phases within the lithium layer. Even a small fraction of 0.02 MCU reduces the average grain width compared to the pristine 20 MCU layer, and increasing the fraction to 0.08 MCU further suppresses grain growth. In this case, grains fail to develop into fully columnar structures, as reflected by the temporal evolution of grain width and height: at 0.08 MCU, the grain height no longer reaches the full layer thickness, indicating the presence of multiple stacked grains. This stagnation results from grain boundary pinning at the particles, which blocks curvature-driven growth in both height and in-plane directions and leads to a plateau in grain size over time.

Fig. 3c examines the influence of substrate microstructure. The attached substrates with average grain sizes of 10 MCU and 30 MCU reveal a reduction in lithium grain size compared to the case without substrate-layer interaction. Here, suppression of columnar growth originates from grain boundary pinning at the substrate rather than dispersed particles. Larger substrate grains result in fewer pinning sites, allowing larger lithium grains. This finding is particularly relevant for bismuth: the presence of a  $\text{Li}_3\text{Bi}$  interlayer at the SE|Li interface alters the substrate and, similar to substrate grain boundaries in the model, is expected to provide additional pinning sites that constrain lithium grain growth. For more information on the substrate microstructure, the pristine interlayers were analyzed by SEM and EBSD (see Fig. S14 and Note S3). All interlayers exhibit nanocrystalline structures with grain diameters below 200 nm and preferred orientation. After lithium plating, the lithium grains are therefore orders of magnitude larger than the substrate grains, suggesting that the layer thickness effect dominates and largely overshadows substrate-related effects. It should be noted, however, that the substrate microstructure may further evolve due to alloy formation. Future work should systematically tailor the substrate grain size to match lithium grain size, ideally using non-alloying substrates to isolate substrate effects, while separately addressing the microstructural evolution of alloying substrates during phase formation.

In addition to the microstructure of the substrate, its roughness can also influence the resulting lithium microstructure, as additional simulations in Fig. S15 show. In the experiment, the different substrate roughness could therefore further influence the lithium microstructure, particularly for bismuth, but also for all interlayers, as they were initially deposited onto the titanium foil. Furthermore, these two substrate effects could explain the slight differences mentioned above in the

microstructures of lithium on steel compared to lithium on titanium. These results highlight the impact of substrate selection on the resulting lithium microstructure. Please note that due to interactions with the substrate, simulation artefacts such as single-voxel grains may occur; therefore, only grains exceeding three voxels in both height and width were considered in the averages shown for the substrate microstructure simulations.

Overall, the simulations demonstrate that layer thickness, secondary particles (*i.e.*, inclusions) and the substrate can significantly affect grain growth dynamics and the resulting lithium microstructure. Enhanced layer thickness leads to larger grains and columnar structures, whereas inclusions and substrate interactions introduce pinning effects that hinder growth and the formation of columnar grain structures. Importantly, the results highlight that interactions with inclusions and the substrate are inevitable in real systems, as otherwise grain growth in 3D will proceed until a single grain is formed due to residual grain curvature.

### Microstructural evolution during lithium stripping

Having shown that interlayers affect the lithium microstructure during the initial deposition, the question remains how the microstructure evolves during subsequent stripping of the electrodeposited lithium layer, both in case of pristine CC foils as well as CCs with an interlayer. Previous work has shown that the microstructure of (pure) lithium is largely determined by the layer thickness.<sup>33,34</sup> Conversely, lithium stripping is expected to lead to a reduction in the average grain width. However, this would mean that existing grains would have to disintegrate, or new grain boundaries would have to be created, which would lead to an increase in energy in the system. Clearly, our knowledge on these microstructure issues is yet poor, and it is important to investigate the microstructural development of lithium during cycling in more detail.

To analyze the microstructural evolution of lithium during and after stripping, a lithium layer with an areal charge of  $10 \text{ mAh cm}^{-2}$  (nominally  $50 \mu\text{m}$ ) was initially electrodeposited. To reduce the risk of dendrite formation at this high areal charge, the used current density was decreased to  $100 \mu\text{A cm}^{-2}$ . After successful electrodeposition,  $5 \text{ mAh cm}^{-2}$  of the  $10 \text{ mAh cm}^{-2}$  were stripped again using a current density of  $100 \mu\text{A cm}^{-2}$  and the remaining lithium layer was analyzed using EBSD in the same way as before. Results of the EBSD analysis are summarized in Fig. 4. The different model systems are schematically shown in Fig. 4a. Additionally, a part of the respective IPF maps and an inverse pole figure, summarizing the orientation of all detected lithium grains is given.

In accordance with Fig. 1, the voltage profiles in Fig. 4b show that in all cases an areal charge of  $10 \text{ mAh cm}^{-2}$  could be deposited without indication of dendrite formation. Interestingly, in this case additional plateaus can be seen in the voltage profile for the silver interlayer. This could be due to the lower deposition current density of  $100 \mu\text{A cm}^{-2}$  instead of  $150 \mu\text{A cm}^{-2}$ . The voltage profile during subsequent stripping of  $5 \text{ mAh cm}^{-2}$  looks similar in all cases. This was to be





**Fig. 4** Microstructure of electrodeposited lithium after partial stripping. (a) Cell setup used for stripping after electrodeposition of  $10 \text{ mAh cm}^{-2}$  of lithium. The location of the interlayers is indicated schematically. (b) Potential profile during electrodeposition of  $10 \text{ mAh cm}^{-2}$  lithium on the left and subsequent stripping of  $5 \text{ mAh cm}^{-2}$  on the right. (c) Microstructure of the partially stripped lithium layers using the different interlayer materials. The IPF maps are given parallel to the  $y$ -direction as indicated above. The shown scalebar resembles  $40 \mu\text{m}$  in all cases. (d) IPFs of the partially stripped lithium layers, showing the distribution of all measured grain orientations. Please note that the IPFs were created based on the entire analyzed cross-section, which is shown in the SI.

expected as no de-alloying takes place and a significant amount of  $5 \text{ mAh cm}^{-2}$  lithium remains after stripping.

The inverse pole figure maps reveal significant microstructural changes during the stripping process. For the pristine titanium foil, the columnar lithium grain microstructure remains intact, similarly to the electrodeposited lithium layer in Fig. 1. However, after stripping nearly all grains exhibit the same orientation, with the  $\langle 101 \rangle$  directions aligned parallel to the  $y$ -axis. This uniform orientation is indicated by the green color of the grains in Fig. 4c and is confirmed by the inverse pole figure, shown in Fig. 4d, which considers the entire cross-section (see Fig. S16). For the inverse pole figures in parallel to the  $x$ - and  $z$ -axis, the reader is referred to Fig. S17. Interestingly, this preferred orientation is the orientation for which Chen *et al.* reported the highest critical current density, which the authors attribute to the lowest migration diffusion barrier and the lowest Young's modulus.<sup>37</sup> Furthermore, when comparing the lithium layer with an areal charge of  $7.5 \text{ mAh cm}^{-2}$  and the one with an absolute areal charge of  $5 \text{ mAh cm}^{-2}$  ( $10 \text{ mAh cm}^{-2}$  plated and  $5 \text{ mAh cm}^{-2}$  stripped), a decrease in the average grain size is seen in Fig. S18. This trend is confirmed when this sample is compared with others subjected to single-step plating for areal charges of  $5 \text{ mAh cm}^{-2}$  and  $10 \text{ mAh cm}^{-2}$  (see Fig. S19). Notably, both samples with an absolute areal charge of  $5 \text{ mAh cm}^{-2}$  exhibit comparable average grain sizes, despite

their different cycling histories. Accordingly, stripping following plating leads to a decrease in the average grain size; apparently *vice versa* to the previously observed grain growth with increasing layer thickness.

For the gold interlayer, the overall decreased grain size and the more distorted lithium microstructure compared to the pristine titanium foil is retained. Here, too, there appears to be a change in the grain orientations with a preference close to the  $\langle 101 \rangle$  direction, as can be seen from the excerpt of the analyzed cross-section shown in Fig. 4c and the inverse pole figure in Fig. 4d. Note that the inverse pole figure takes into account the whole cross-section displayed in Fig. S20. In contrast to titanium foil, however, there appears to be an increase in the average grain size during the stripping process, and not the decrease in grain size clearly observed with titanium (revisit Fig. S18).

In the case of silver, similar to gold, a reduced average grain size can be seen compared to the pristine titanium foil. A change in grain orientation is not as obvious as in the previous samples. Although the orientation of the  $7.5 \text{ mAh cm}^{-2}$  lithium layer plated on silver differs from the one shown here, no preferential orientation is recognizable after stripping on the whole cross-section in Fig. S21. As with gold, a higher average grain size can be seen in the box plot in Fig. S18 in the case of the stripped silver sample ( $10 \text{ mAh cm}^{-2}$  plating followed by



5 mAh cm<sup>-2</sup> stripping) compared to the sample solely plated (7.5 mAh cm<sup>-2</sup> plating). In addition, another lithium layer with an areal charge of 7.5 mAh cm<sup>-2</sup> was deposited onto a silver interlayer, of which 3 mAh cm<sup>-2</sup> was then stripped again (see Fig. S22). Here, too, the average grain size is slightly higher for the sample which was partially stripped compared to the one subjected to a single-plating step.

Finally, the stripped lithium layer with a bismuth interlayer shows a more distorted microstructure compared to the bismuth sample previously analyzed after electrodeposition as well as the pristine titanium foil samples. While a preferential orientation of the lithium layer solely plated on a bismuth interlayer could be found (compare Fig. 1) – which is mainly due to very large individual grains – no preferential orientation of the stripped lithium layer with a bismuth interlayer is visible when analyzing the full cross-section in Fig. S23. Furthermore, a significant decrease in the average grain size of the lithium layer is visible when comparing the sample which was stripped after plating with the solely plated one using a bismuth interlayer, as can be seen in the box plot in Fig. S18. Interestingly, there are no longer any particularly large grains to be found. On the contrary, there is an area within the lithium layer that appears to be particularly disordered and to consist of many small grains. Please note that these particularly small grains were not included in the quantification of the mean grain width, as neighboring grains cannot always reliably be distinguished from one another in this area with the chosen measurement resolution.

In addition to the different microstructures found after electrodeposition, the choice of interlayers also appears to influence stripping performance and lithium microstructure evolution. For the pristine titanium foil and the titanium foil with a bismuth interlayer, unlike gold and silver interlayers, the average grain size decreases again during stripping, likely because the lithium layers remain chemically pure. Thus, it appears that the recently found layer thickness effect for lithium is reversible, potentially driven by external pressure forming new grains and grain boundaries during stripping. On the other hand, in the case of gold, Li<sub>15</sub>Au<sub>4</sub> particles are found inside the lithium layer, while in the case of silver, dissolved silver is present. These lithium layers are therefore no longer chemically pure as the first plating step causes alloying with the interlayer element. Already during the investigation of the deposited lithium layers, it could be shown that these interlayer elements significantly change or suppress the grain growth within the lithium layers. Accordingly, the results obtained here suggest that the microstructural changes taking place in the pure lithium layers during stripping are suppressed in a similar way. Under this assumption, the microstructure of the lithium layers is “frozen” at an areal charge of 10 mAh cm<sup>-2</sup> and thus an increase in the average grain size compared to the layers at an areal charge of 7.5 mAh cm<sup>-2</sup> is to be expected. This hypothesis is further supported by the silver layer mentioned above, in which after a deposition of 7.5 mAh cm<sup>-2</sup>, 3 mAh cm<sup>-2</sup> were stripped and yet a similar grain size was observed. The reason for the lack of microstructural changes in

the gold and silver interlayers could be the reduced grain boundary mobility or changed mechanical properties, such as alloy hardening, which means that the external driving force, the pressure applied, is no longer sufficient to cause these changes.

### Microstructural evolution during cycling

To investigate the effect of cycling on the lithium microstructure, cells were cycled using a silver interlayer, which prevented the short-circuiting observed in cells without interlayer and allowed stable lithium deposition. In these experiments, 4.5 mAh cm<sup>-2</sup> of lithium was plated and stripped for ten cycles with a cutoff potential of 50 mV, ending with the 10th deposition step. The initial plating step was carried out at reduced current density to ensure that lithium deposition occurred only after complete alloy formation. Cycling results together with EBSD analysis after the final deposition step using a silver interlayer are shown in Fig. 5.

During the first plating step in Fig. 5a, several plateaus can be seen in the voltage curve, which are due to alloy formation. As cycling progresses, increasingly large (nucleation) overpotentials occur at the beginning of plating. We attribute this to an inhomogeneous silver distribution at higher cycle numbers. The absence of silver causes lithium nucleation at the bare titanium CC, resulting in the increasing nucleation overpotential.<sup>19,29</sup> The increasing IR drop of LPSCl, indicating a higher cell resistance, is likely due to an increasing layer thickness of the SEI over time.<sup>63,64</sup> Furthermore, mechanical degradation of the SEI or the LPSCl itself due to the volume change could lead to a partial loss of contact with the electrode and thus to higher constriction resistances.<sup>65</sup> Morphological analysis of the electrode following cycling in Fig. 5b shows that mechanical damage must have indeed occurred to the SE or the SEI, as LPSCl residues are found on the titanium electrode and within the lithium layer. This is accompanied by a decrease in the amount of deposited lithium that can be stripped again. As evident from the stripping curves, it is in the range of 90–95% of the plated amount and decreases with increasing cycle number.

Analysis of the lithium grains in Fig. 5c shows a clear deviation from a columnar structure after repeated deposition and dissolution. In contrast to the mostly uniform columnar structure observed after single dissolution, only three columnar grains remain, while numerous smaller grains emerge between them. This finer-grained microstructure may result from variations in interfacial energy at the Li|LPSCl interface as SEI thickness increases. More likely, however, is an influence of the observed mechanical degradation of the SEI or LPSCl during cycling, which introduces secondary phases into the layer. In line with our experimental findings with gold interlayers and our simulation results, secondary phases can impede grain growth and thereby decrease the grain size. In addition, the LPSCl residues on the titanium foil also lead to an increased roughness of the deposited lithium layer, which in turn was identified in our simulations as additional factor influencing the resulting microstructure. A contribution from



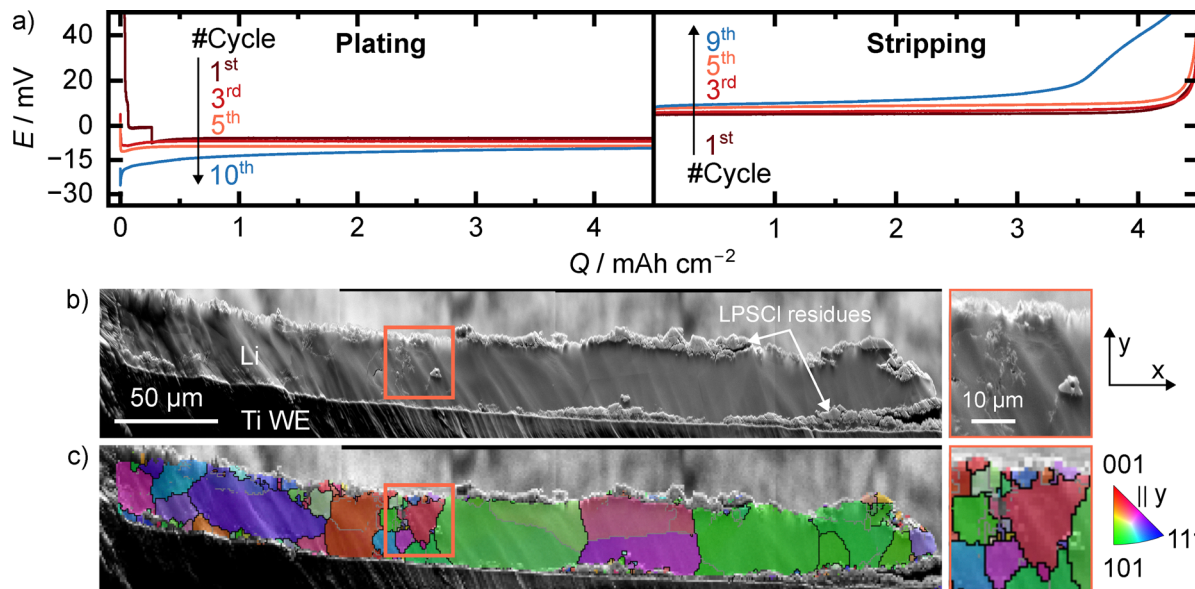


Fig. 5 Cycling results for repeated lithium plating and stripping on a silver interlayer. (a) Plating and stripping curves during lithium cycling. (b) SEM image of the lithium layer following the cycling experiment. (c) Overlay of the SEM image with the IPF map. The IPF map is given parallel to the  $y$ -direction as indicated on the right. To the right of (b) and (c), an enlarged section of the respective image is shown.

silver particles at low areal charges also cannot be excluded as full silver dissolution is expected only after  $\sim 4.2 \text{ mAh cm}^{-2}$  of lithium deposition.

Overall, these observations highlight that the lithium microstructure during cycling is influenced by multiple complex and interdependent factors. While alloying with the silver interlayer enables stable cycling, repeated plating and stripping leads to mechanical degradation of the SEI and SE, secondary phase dispersion, and increasing roughness. These changes alter the lithium grains simultaneously, resulting in a finer, less columnar microstructure over time. This underscores that lithium microstructure is highly sensitive to the underwent cycling history and interfacial dynamics, emphasizing the need to consider multiple coupled mechanisms when investigating the lithium microstructure *post mortem*.

### Interlayers in reservoir-free lithium cells

In the following, the observations made on the influence of gold, silver and bismuth interlayers on the resulting microstructure of plated and stripped lithium layers from the previous chapters are discussed in detail. The schematic in Fig. 6 serves as a graphical summary.

At the beginning of plating, depending on the binary phase diagram of the interlayer material and lithium, alloy formation and subsequent nucleation of lithium take place. While nucleation occurs at the Ti|LPSCl interface for the pristine titanium foil, in the case of gold and silver lithium nucleates at the interface between the forming gold–lithium or silver–lithium alloy and LPSCl, respectively. For bismuth, a bismuth–lithium alloy also forms first. According to the experiments presented, lithium nucleates between this alloy and the titanium foil.

With continuous lithium plating, the increasing layer thickness also leads to an increase in the lithium grain width, which is consistent with previous experimental and simulation results. For the pristine titanium foil, distinctive columnar lithium grains are formed, which have a width corresponding to approximately twice their height, which has already been observed for lithium layers plated at steel|LPSCl interfaces.<sup>34</sup>

As shown schematically in Fig. 6a, volume expansion during lithium plating can lead to the dispersion of secondary phases. For example, in the case of gold interlayers, alloy particles ( $\text{Li}_{15}\text{Au}_4$ ) can be found in the lithium layer. These lead to a more disordered microstructure and smaller grain size within the lithium layer, deviating from the columnar structure previously observed in chemically pure lithium layers. We assume that these differences are caused by the alloy particles mentioned *via* a mechanism similar to Zener pinning, *i.e.*, the grain boundary mobility is reduced, grain boundaries can be pinned to the particles and thus grain growth is prevented or restricted. These assumptions are underpinned by our simulation, showing a decreased grain size as well as multiple layers of grains when secondary particles are present. We like to emphasize that similar effects can also be caused by electrochemically inactive secondary phases, such as solid electrolyte (interphase) fragments. Therefore, electrolyte choice (both liquid and solid) can affect microstructure development through its mechanical properties and SEI formation.

Furthermore, as in the case of silver and shown in Fig. 6b, complete interlayer dissolution may occur in the course of lithium plating. This also leads to modification of the lithium microstructure. Compared to gold, however, the columnar structure of the lithium grains known from electrodeposition on pristine titanium or steel appears to be largely preserved,





**Fig. 6** Microstructural effects of interlayers in reservoir-free solid-state batteries. The model system used is shown schematically on the left. Depending on the phase diagram, different alloy reactions including (a) secondary phase formation, (b) interlayer dissolution and (c) phase separation can occur during ongoing lithium electrodeposition. These can improve the cycling stability by (d) increasing the current collector (CC) coverage, (e) mitigating pore formation and (f) altering the resulting lithium microstructure.

albeit with a significantly lower aspect ratio, *i.e.*, there are more grains that are taller than they are wide. Since lithium has residual solubility for silver and, in the samples examined here, silver is completely dissolved in lithium, a mechanism similar to Zener pinning seems unlikely at the point of examination. Instead, based on our XRD results for a Li(Ag) solid solution produced from melt, we assume that the dissolved silver induces lattice strain by changing lattice parameters, thereby causing the observed changes in microstructure. At this point, we like to mention that an additional mechanism similar to Zener pinning is likely to occur until all silver is completely dissolved in lithium.

Finally, phase separation may occur. This is shown in Fig. 6c and was observed for bismuth interlayers as an example. Here, the columnar structure of the lithium grains is largely preserved during plating. However, compared to the pristine titanium foil, the grain width appears to be even wider, with some grains that have grown particularly large, which could indicate abnormal grain growth. We assume that this is due to the deposition of lithium between the bismuth–lithium alloy and the titanium foil. As a result, the substrate differs and there is no direct contact between lithium and LPSCl. The Li|LPSCl interface alters the resulting lithium microstructure,<sup>34</sup> leading for example to the formation of truncated grains, as also found in Fig. 1c in this study. Without this interaction, it is conceivable that the grains could grow even wider. In addition, faster diffusion of lithium along the bismuth–lithium alloy could lead to the formation of larger grains.

In line with literature, interlayers can lead to improved cycling stability. This is caused, among other effects, by an increased CC coverage and a mitigated pore formation,<sup>10,13,20,25,31</sup> as schematically illustrated in Fig. 6d and e. While these concepts have already been frequently observed and discussed in the literature, an altered microstructure is emerging as an additional influencing factor when using interlayers in RFCs, as shown in Fig. 6f. Specifically, the presence of interlayers can lead to a reduction in lithium grain size, as observed for gold and silver, which increases the density of grain boundaries within the plated layer. This, in turn, provides additional pathways for lithium diffusion.<sup>31,35</sup> Translating these fundamental insights into design principles, our results indicate that interlayers resulting in a finer lithium grain structure, such as gold and silver, are preferable for enabling stable cycling in RFCs. The combination of smaller grain size, theoretically linked to enhanced diffusivity, and the experimentally observed higher initial CC coverage suggests that these metals facilitate more homogeneous lithium cycling than bismuth. However, it should be noted that in addition to the reduced grain size, the introduction of alloy phases with improved diffusion properties, as previously reported for Li<sub>3</sub>Bi, likely also contributes to improved cycling stability.<sup>57</sup>

Furthermore, our experimental results reveal for the first time that cycling itself significantly alters the lithium microstructure, too. For the pristine titanium foil, it was shown that, with decreasing layer thickness, the average grain size decreases again. Thus, the previously observed layer thickness



effect appears to be reversible.<sup>34</sup> In addition, in the case of pristine titanium, a strongly pronounced preferred orientation of the lithium grains occurs, which, following stripping, almost exclusively exhibit a  $\langle 101 \rangle$  orientation parallel to the stripping direction. In contrast, the gold and silver interlayers appear to slow down grain boundary movement, and thus, the reversible growth and shrinkage of grains with layer thickness is suppressed. The lithium layer formed by plating  $10 \text{ mAh cm}^{-2}$  and stripping  $5 \text{ mAh cm}^{-2}$  has a larger average grain width than the layer formed by directly plating  $7.5 \text{ mAh cm}^{-2}$ . Accordingly, we assume that in this case, when analyzing the sample, we still see the grain microstructure that developed during the deposition of the  $10 \text{ mAh cm}^{-2}$ . The Zener pinning of the gold alloy particles or the lattice strain within the  $\text{Li(Ag)}$  solid solution prevents the expected decrease in grain size during stripping. For gold and silver, a well defined preferred orientation during stripping is also lacking. Although a slight change in orientation appears to occur here as well, it is less pronounced than in the case of the pristine titanium foil. Similarly, a preferred orientation is also lacking for the bismuth interlayer. However, a decrease in the mean grain size following stripping is again evident here. We assume that the reversible change of grain size with the layer thickness occurs also here, as in the case of titanium, since both cases involve chemically pure lithium and only the substrate differs. Interestingly, some very small grains with a more disordered microstructure were found for the bismuth interlayer following stripping, in contrast to the results after plating. We hypothesize that these areas could be areas where particularly large, possibly abnormally grown grains were previously located. During stripping, these then disintegrate into many smaller grains. In general, the cycling history also plays an important role in the resulting microstructure of lithium. This was further confirmed by first cycling experiments. In addition to the influencing factors already discussed, the mechanical degradation of the SE and the associated contamination of the lithium layer were identified as additional factors.

## Conclusions

In this study, we deepen the understanding of how thin alloying interlayers affect the microstructure of electrodeposited lithium layers in reservoir-free produced SSBs, using EBSD on wide cross-sections prepared *via* broad ion beam milling. Lithium deposited on gold and silver interlayers exhibit a microstructure with a reduced grain size compared to lithium deposited at the titanium foil reference. The columnar structure with low-aspect ratio grains found for various metal CCs also vanishes when gold and silver are used. In contrast, the columnar structure of lithium layers deposited on bismuth interlayers is largely preserved with even increased grain size compared to lithium electrodeposited on pristine titanium foils. The smaller grain size should improve cycling for both gold and silver interlayers, with the effect for silver potentially being stronger due to its more uniform distribution within the lithium layer.

Additional EDS and EBSD analysis of the cross-sections provided information on the different modes of action of the interlayers. Gold and silver interlayers ensure that the deposited lithium is no longer chemically pure, which in turn suppresses grain growth. The bismuth interlayer, on the other hand, separates the lithium layer from the solid electrolyte LPSCl used here and thus changes the substrate and therefore the microstructure of the deposited lithium.

In addition, the microstructural change of remaining lithium caused by stripping of previously plated lithium was analyzed for the first time. In the case of chemically pure lithium, *i.e.*, pristine titanium foil and the bismuth interlayer, a reduction of the mean grain size could be observed, which shows that the previously observed layer thickness effect for plated lithium is reversible. In the case of gold and silver interlayers, however, this reversibility appears to be largely prevented and no decrease in grain size was observed during stripping. Interestingly, in the case of stripping lithium on titanium, a strong preferential orientation of the remaining lithium grains was also detected. Thus, in addition to alloying interlayer materials, the cycling history of LMEs can be identified as an influencing factor on the lithium microstructure. This is particularly evident in the lithium analyzed after cycling. Overall, our results emphasize that an “electrometallurgical” understanding is needed to describe the dynamic microstructural changes in LMEs during cycling and that additional microstructure analysis during cycling is necessary, especially when using interlayers.

## Author contributions

The author contributions are given based on the contributor roles taxonomy (CRediT): J. B.: conceptualization, methodology, investigation, validation, formal analysis, writing – original draft, visualization, writing – review & editing; L. S.: conceptualization, methodology, investigation, validation, formal analysis, visualization, writing – review & editing; S. K.: formal analysis, software, visualization, writing – review & editing; T. F.: conceptualization, formal analysis, methodology, supervision, visualization, writing – review & editing; J. J.: conceptualization, methodology, resources, supervision, writing – original draft, writing – review & editing, and funding acquisition.

## Conflicts of interest

The authors declare no competing interests.

## Data availability

Data for this article, including electrochemical and EBSD data are available at “JLUPub” at <https://doi.org/10.22029/jlupub-20276>.

The SI contains figures (Fig. S1–S23) and notes (Note S1–S4). See DOI: <https://doi.org/10.1039/d5ee07230a>.



## Acknowledgements

The authors acknowledge funding by Evonik Operations GmbH. This work has also been partly funded by the German Federal Ministry of Education and Research (BMBF) within the DE-US program under the project “LiSI2”, grant identifier 03XP0509B, as well as the cluster of competence “FestBatt”, grant identifier 03XP0428E. The responsibility for the content of this publication lies with the authors. The authors thank Daniel Wagner for his support in analysis of the XRD data.

## References

- J. Janek and W. G. Zeier, A Solid Future for Battery Development, *Nat. Energy*, 2016, **1**(9), 16141, DOI: [10.1038/nenergy.2016.141](https://doi.org/10.1038/nenergy.2016.141).
- T. Krauskopf, F. H. Richter, W. G. Zeier and J. Janek, Physicochemical Concepts of the Lithium Metal Anode in Solid-State Batteries, *Chem. Rev.*, 2020, **120**(15), 7745–7794, DOI: [10.1021/acs.chemrev.0c00431](https://doi.org/10.1021/acs.chemrev.0c00431).
- P. Albertus, S. Babinec, S. Litzelman and A. Newman, Status and Challenges in Enabling the Lithium Metal Electrode for High-Energy and Low-Cost Rechargeable Batteries, *Nat. Energy*, 2018, **3**(1), 16–21, DOI: [10.1038/s41560-017-0047-2](https://doi.org/10.1038/s41560-017-0047-2).
- S. K. Otto, Y. Moryson, T. Krauskopf, K. Peppler, J. Sann, J. Janek and A. Henss, In-Depth Characterization of Lithium-Metal Surfaces with XPS and ToF-SIMS: Toward Better Understanding of the Passivation Layer, *Chem. Mater.*, 2021, **33**(3), 859–867, DOI: [10.1021/acs.chemmater.0c03518](https://doi.org/10.1021/acs.chemmater.0c03518).
- S. K. Otto, T. Fuchs, Y. Moryson, C. Lerch, B. Mogwitz, J. Sann, J. Janek and A. Henss, Storage of Lithium Metal: The Role of the Native Passivation Layer for the Anode Interface Resistance in Solid State Batteries, *ACS Appl. Energy Mater.*, 2021, **4**(11), 12798–12807, DOI: [10.1021/acsaem.1c02481](https://doi.org/10.1021/acsaem.1c02481).
- M. Burton, S. Narayanan, B. Jagger, L. F. Olbrich, S. Dhir, M. Shibata, M. J. Lain, R. Astbury, N. Butcher, M. Copley, T. Kotaka, Y. Aihara and M. Pasta, Techno-Economic Assessment of Thin Lithium Metal Anodes for Solid-State Batteries, *Nat. Energy*, 2024, **10**(1), 135–147, DOI: [10.1038/s41560-024-01676-7](https://doi.org/10.1038/s41560-024-01676-7).
- K. B. Hatzell, X. C. Chen, C. L. Cobb, N. P. Dasgupta, M. B. Dixit, L. E. Marbella, M. T. McDowell, P. P. Mukherjee, A. Verma, V. Viswanathan, A. S. Westover and W. G. Zeier, Challenges in Lithium Metal Anodes for Solid-State Batteries, *ACS Energy Lett.*, 2020, **9**(2), 922–934, DOI: [10.1021/acseenergylett.9b02668](https://doi.org/10.1021/acseenergylett.9b02668).
- M. J. Wang, E. Carmona, A. Gupta, P. Albertus and J. Sakamoto, Enabling “Lithium-Free” Manufacturing of Pure Lithium Metal Solid-State Batteries through in Situ Plating, *Nat. Commun.*, 2020, **11**(1), 1–9, DOI: [10.1038/s41467-020-19004-4](https://doi.org/10.1038/s41467-020-19004-4).
- S. E. Sandoval, C. G. Haslam, B. S. Vishnugopi, D. W. Liao, J. S. Yoon, S. H. Park, Y. Wang, D. Mitlin, K. B. Hatzell, D. J. Siegel, P. P. Mukherjee, N. P. Dasgupta, J. Sakamoto and M. T. McDowell, Electro-Chemo-Mechanics of Anode-Free Solid-State Batteries, *Nat. Mater.*, 2025, **24**(5), 673–681, DOI: [10.1038/s41563-024-02055-z](https://doi.org/10.1038/s41563-024-02055-z).
- S. E. Sandoval, J. A. Lewis, B. S. Vishnugopi, D. L. Nelson, M. M. Schneider, F. J. Q. Cortes, C. M. Matthews, J. Watt, M. Tian, P. Shevchenko, P. P. Mukherjee and M. T. McDowell, Structural and Electrochemical Evolution of Alloy Interfacial Layers in Anode-Free Solid-State Batteries, *Joule*, 2023, **7**(9), 2054–2073, DOI: [10.1016/j.joule.2023.07.022](https://doi.org/10.1016/j.joule.2023.07.022).
- C. G. Haslam, J. K. Eckhardt, A. Ayyaswamy, B. S. Vishnugopi, T. Fuchs, D. W. Liao, N. P. Dasgupta, P. P. Mukherjee, J. Janek and J. Sakamoto, Evaluating Pressure-Dependent Discharge Behavior of Foil Versus In Situ Plated Lithium Metal Anodes in Solid-State Batteries, *Adv. Energy Mater.*, 2024, **15**(12), 2403614, DOI: [10.1002/aenm.202403614](https://doi.org/10.1002/aenm.202403614).
- J. Becker, T. Weintraut, S. L. Benz, T. Fuchs, C. Lerch, P. Becker, J. K. Eckhardt, A. Henß, F. H. Richter and J. Janek, Purity of Lithium Metal Electrode and Its Impact on Lithium Stripping in Solid-State Batteries, *Nat. Commun.*, 2025, **16**(1), 5395, DOI: [10.1038/s41467-025-61006-7](https://doi.org/10.1038/s41467-025-61006-7).
- T. Krauskopf, R. Dippel, H. Hartmann, K. Peppler, B. Mogwitz, F. H. Richter, W. G. Zeier and J. Janek, Lithium-Metal Growth Kinetics on LLZO Garnet-Type Solid Electrolytes, *Joule*, 2019, **3**(8), 2030–2049, DOI: [10.1016/j.joule.2019.06.013](https://doi.org/10.1016/j.joule.2019.06.013).
- M. Motoyama, M. Ejiri and Y. Iriyama, In-Situ Electron Microscope Observations of Electrochemical Li Deposition/Dissolution with a LiPON Electrolyte, *Electrochemistry*, 2014, **82**(5), 364–368, DOI: [10.5796/electrochemistry.82.364](https://doi.org/10.5796/electrochemistry.82.364).
- E. Kazyak, M. J. Wang, K. Lee, S. Yadavalli, A. J. Sanchez, M. D. Thouless, J. Sakamoto and N. P. Dasgupta, Understanding the Electro-Chemo-Mechanics of Li Plating in Anode-Free Solid-State Batteries with Operando 3D Microscopy, *Matter*, 2022, **5**(11), 3912–3934, DOI: [10.1016/j.matt.2022.07.020](https://doi.org/10.1016/j.matt.2022.07.020).
- T. Krauskopf, H. Hartmann, W. G. Zeier and J. Janek, Toward a Fundamental Understanding of the Lithium Metal Anode in Solid-State Batteries—An Electrochemo-Mechanical Study on the Garnet-Type Solid Electrolyte  $\text{Li}_{6.25}\text{Al}_{0.25}\text{La}_3\text{Zr}_2\text{O}_{12}$ , *ACS Appl. Mater. Interfaces*, 2019, **11**(15), 14463–14477, DOI: [10.1021/acsami.9b02537](https://doi.org/10.1021/acsami.9b02537).
- D. K. Singh, T. Fuchs, C. Krempaszky, B. Mogwitz, S. Burkhardt, F. H. Richter and J. Janek, Overcoming Anode Instability in Solid-State Batteries through Control of the Lithium Metal Microstructure, *Adv. Funct. Mater.*, 2023, **33**(1), 2211067, DOI: [10.1002/adfm.202211067](https://doi.org/10.1002/adfm.202211067).
- T. Fuchs, C. G. Haslam, A. C. Moy, C. Lerch, T. Krauskopf, J. Sakamoto, F. H. Richter and J. Janek, Increasing the Pressure-Free Stripping Capacity of the Lithium Metal Anode in Solid-State-Batteries by Carbon Nanotubes, *Adv. Energy Mater.*, 2022, **12**(26), 2201125, DOI: [10.1002/aenm.202201125](https://doi.org/10.1002/aenm.202201125).
- Y.-G. Lee, S. Fujiki, C. Jung, N. Suzuki, N. Yashiro, R. Omoda, D.-S. Ko, T. Shiratsuchi, T. Sugimoto, S. Ryu, J. H. Ku, T. Watanabe, Y. Park, Y. Aihara, D. Im and I. T. Han, High-Energy Long-Cycling All-Solid-State Lithium Metal Batteries Enabled by Silver–Carbon Composite



- Anodes, *Nat. Energy*, 2020, 5(4), 299–308, DOI: [10.1038/s41560-020-0575-z](https://doi.org/10.1038/s41560-020-0575-z).
- 20 C. Haslam and J. Sakamoto, Stable Lithium Plating in “Lithium Metal-Free” Solid-State Batteries Enabled by Seeded Lithium Nucleation, *J. Electrochem. Soc.*, 2023, 170(4), 040524, DOI: [10.1149/1945-7111/accab4](https://doi.org/10.1149/1945-7111/accab4).
- 21 D. Lin, Y. Liu, Z. Liang, H. W. Lee, J. Sun, H. Wang, K. Yan, J. Xie and Y. Cui, Layered Reduced Graphene Oxide with Nanoscale Interlayer Gaps as a Stable Host for Lithium Metal Anodes, *Nat. Nanotechnol.*, 2016, 11(7), 626–632, DOI: [10.1038/nnano.2016.32](https://doi.org/10.1038/nnano.2016.32).
- 22 F. Xie, M. S. Diallo, H. Kim, Q. H. Tu and G. Ceder, The Microscopic Mechanism of Lithiation and Delithiation in the Ag/C Buffer Layer for Anode-Free Solid-State Batteries, *Adv. Energy Mater.*, 2024, 14(10), 2302960, DOI: [10.1002/aenm.202302960](https://doi.org/10.1002/aenm.202302960).
- 23 S. H. Park, K. G. Naik, B. S. Vishnugopi, P. P. Mukherjee and K. B. Hatzell, Lithium Kinetics in Ag–C Porous Interlayer in Reservoir-Free Solid-State Batteries, *Adv. Energy Mater.*, 2024, 15(16), 2405129, DOI: [10.1002/aenm.202405129](https://doi.org/10.1002/aenm.202405129).
- 24 D.-S. Ko, S. Kim, S. Lee, G. Yoon, D. Kim, C. Shin, D. Kim, J. Lee, S. Sul, D.-J. Yun and C. Jung, Mechanism of Stable Lithium Plating and Stripping in a Metal-Interlayer-Inserted Anode-Less Solid-State Lithium Metal Battery, *Nat. Commun.*, 2025, 16(1), 1066, DOI: [10.1038/s41467-025-55821-1](https://doi.org/10.1038/s41467-025-55821-1).
- 25 Y. Wang, Y. Liu, M. Nguyen, J. Cho, N. Katyal, B. S. Vishnugopi, H. Hao, R. Fang, N. Wu, P. Liu, P. P. Mukherjee, J. Nanda, G. Henkelman, J. Watt and D. Mitlin, Stable Anode-Free All-Solid-State Lithium Battery through Tuned Metal Wetting on the Copper Current Collector, *Adv. Mater.*, 2023, 35(8), 2206762, DOI: [10.1002/adma.202206762](https://doi.org/10.1002/adma.202206762).
- 26 M. Motoyama, K. Shimizu, T. Kimura, T. Yamamoto, S. Watanabe and Y. Iriyama, Uncovering the Dynamics of Li–Au Alloying and Li Nucleation at the Au/LiPON Interface with In Situ Z Contrast and Surface Roughness Contrast Imaging via Scanning Electron Microscopy, *JACS Au*, 2024, 4(12), 4700–4714, DOI: [10.1021/jacsau.4c00530](https://doi.org/10.1021/jacsau.4c00530).
- 27 M. An, H. Wang, W. Cheng, G. Li, S. Liu and X. Gao, Li–Bi and Li–In Alloys-Based Composite Anode for Lithium Metal Batteries, *J. Alloys Compd.*, 2023, 966, 171619, DOI: [10.1016/j.jallcom.2023.171619](https://doi.org/10.1016/j.jallcom.2023.171619).
- 28 D. Spencer-Jolly, V. Agarwal, C. Doerrer, B. Hu, S. Zhang, D. L. R. Melvin, H. Gao, X. Gao, P. Adamson, O. V. Magdysyuk, P. S. Grant, R. A. House and P. G. Bruce, Structural Changes in the Silver–Carbon Composite Anode Interlayer of Solid-State Batteries, *Joule*, 2023, 7(3), 503–514, DOI: [10.1016/j.joule.2023.02.001](https://doi.org/10.1016/j.joule.2023.02.001).
- 29 S. Zhang, G. Yang, Z. Liu, S. Weng, X. Li, X. Wang, Y. Gao, Z. Wang and L. Chen, Phase Diagram Determined Lithium Plating/Stripping Behaviors on Lithiophilic Substrates, *ACS Energy Lett.*, 2021, 6(11), 4118–4126, DOI: [10.1021/acscenergylett.1c02127](https://doi.org/10.1021/acscenergylett.1c02127).
- 30 L. Kalarasse, B. Bennecer and F. Kalarasse, Elastic and Electronic Properties of the Alkali Pnictide Compounds Li<sub>3</sub>Sb, Li<sub>3</sub>Bi, Li<sub>2</sub>NaSb and Li<sub>2</sub>NaBi, *Comput. Mater. Sci.*, 2011, 50(10), 2880–2885, DOI: [10.1016/j.commatsci.2011.05.003](https://doi.org/10.1016/j.commatsci.2011.05.003).
- 31 C. G. Haslam, T. Fuchs, D. W. Liao, J. Becker, N. P. Dasgupta, J. Janek and J. Sakamoto, The Effect of Alloying Interlayers on Lithium Anode Morphology and Microstructure in “Anode-Free” Solid-State Batteries, *ACS Energy Lett.*, 2025, 2285–2291, DOI: [10.1021/acscenergylett.5c00149](https://doi.org/10.1021/acscenergylett.5c00149).
- 32 S. E. Sandoval and M. T. McDowell, Lithium Metal Anodes in Solid-State Batteries: Metal Microstructure Matters, *Matter*, 2023, 2101–2102, DOI: [10.1016/j.matt.2023.05.017](https://doi.org/10.1016/j.matt.2023.05.017).
- 33 T. Fuchs, T. Ortmann, J. Becker, C. G. Haslam, M. Ziegler, V. K. Singh, M. Rohnke, B. Mogwitz, K. Peppler, L. F. Nazar, J. Sakamoto and J. Janek, Imaging the Microstructure of Lithium and Sodium Metal in Anode-Free Solid-State Batteries Using Electron Backscatter Diffraction, *Nat. Mater.*, 2024, 23(12), 1678–1685, DOI: [10.1038/s41563-024-02006-8](https://doi.org/10.1038/s41563-024-02006-8).
- 34 J. Becker, T. Fuchs, T. Ortmann, S. Kremer, F. H. Richter and J. Janek, Microstructure of Lithium Metal Electrodeposited at the Steel|Li<sub>6</sub>PS<sub>5</sub>Cl Interface in “Anode-Free” Solid-State Batteries, *Adv. Energy Mater.*, 2025, 15(16), 2404975, DOI: [10.1002/aenm.202404975](https://doi.org/10.1002/aenm.202404975).
- 35 J. S. Yoon, H. Sulaimon and D. J. Siegel, Exploiting Grain Boundary Diffusion to Minimize Dendrite Formation in Lithium Metal–Solid State Batteries, *J. Mater. Chem. A*, 2023, 11(43), 23288–23299, DOI: [10.1039/D3TA03814A](https://doi.org/10.1039/D3TA03814A).
- 36 J. Becker, T. Fuchs, T. Ortmann, L. Schuster, S. Kremer, F. H. Richter and J. Janek, Analysis of the Microstructural Evolution of Lithium Metal during Electrodeposition and Subsequent Dissolution in “Anode-Free” Solid-State Batteries Using Electron-Backscatter Diffraction on Millimeter-Sized Cross-Sections, *Microscopy and Microanalysis*, Oxford University Press (OUP), 2025, vol. 31, DOI: [10.1093/mam/ozaf048.642](https://doi.org/10.1093/mam/ozaf048.642).
- 37 H. Chen, Y. Zhao, X. Zhang, R. Li, A. Wang, H. Zhang, J. Liu, B. Wen, L. Zhang, Q. Hua, T. Liu, K. Wu, K. Amine and J. Luo, Synthesis of Monocrystalline Lithium for High-Critical-Current-Density Solid-State Batteries, *Nat. Synth.*, 2025, 4(5), 552–561, DOI: [10.1038/s44160-024-00712-4](https://doi.org/10.1038/s44160-024-00712-4).
- 38 O. Seunghyun, S. An and M. Jung, US 2025/0219131 A1, 2025. <https://patents.justia.com/patent/20250219131?utm> (accessed 2025-10-06).
- 39 D. Zöllner and P. Streitenberger, Three-Dimensional Normal Grain Growth: Monte Carlo Potts Model Simulation and Analytical Mean Field Theory, *Scr. Mater.*, 2006, 54(9), 1697–1702, DOI: [10.1016/j.scriptamat.2005.12.042](https://doi.org/10.1016/j.scriptamat.2005.12.042).
- 40 D. Zöllner, A Potts Model for Junction Limited Grain Growth, *Comput. Mater. Sci.*, 2011, 50(9), 2712–2719, DOI: [10.1016/j.commatsci.2011.04.024](https://doi.org/10.1016/j.commatsci.2011.04.024).
- 41 D. Zöllner and I. Zlotnikov, Texture Controlled Grain Growth in Thin Films Studied by 3D Potts Model, *Adv. Theory Simul.*, 2019, 2(8), 1900064, DOI: [10.1002/adts.201900064](https://doi.org/10.1002/adts.201900064).
- 42 D. Zöllner, Treating Grain Growth in Thin Films in Three Dimensions: A Simulation Study, *Comput. Mater. Sci.*, 2016, 125, 51–60, DOI: [10.1016/j.commatsci.2016.08.026](https://doi.org/10.1016/j.commatsci.2016.08.026).
- 43 D. Zöllner and W. Pantleon, Grain Growth in Thin Films – When the Third Dimension Matters, *Comput. Mater. Sci.*, 2025, 258, 114055, DOI: [10.1016/j.commatsci.2025.114055](https://doi.org/10.1016/j.commatsci.2025.114055).



- 44 D. Zöllner and W. Pantleon, Effect of Boundary Grooving on Grain Growth by Potts Model Simulations, *Journal of Physics: Conference Series*, Institute of Physics, 2023, vol. 2635, DOI: [10.1088/1742-6596/2635/1/012033](https://doi.org/10.1088/1742-6596/2635/1/012033).
- 45 W. E. Frazier, S. Hu and V. V. Joshi, A Potts Model Parameter Study of Particle Size, Monte Carlo Temperature, and “Particle-Assisted Abnormal Grain Growth”, *Comput. Mater. Sci.*, 2020, **185**, 109945, DOI: [10.1016/j.commatsci.2020.109945](https://doi.org/10.1016/j.commatsci.2020.109945).
- 46 D. Raabe, Scaling Monte Carlo Kinetics of the Potts Model Using Rate Theory, *Acta Mater.*, 2000, **48**(7), 1617–1628, DOI: [10.1016/S1359-6454\(99\)00451-6](https://doi.org/10.1016/S1359-6454(99)00451-6).
- 47 S. Ling and M. P. Anderson, Monte Carlo Simulation of Grain Growth and Recrystallization in Polycrystalline Materials, *JOM*, 1992, **44**(9), 30–36, DOI: [10.1007/BF03222323](https://doi.org/10.1007/BF03222323).
- 48 S. A. Wright, S. J. Plimpton and T. P. Swiler, *Potts-Model Grain Growth Simulations: Parallel Algorithms and Applications*, Albuquerque, NM, and Livermore, CA (United States), 1997, DOI: [10.2172/522745](https://doi.org/10.2172/522745).
- 49 O. M. Ivasishin, S. V. Shevchenko, N. L. Vasiliev and S. L. Semiatin, 3D Monte-Carlo Simulation of Texture-Controlled Grain Growth, *Acta Mater.*, 2003, **51**(4), 1019–1034, DOI: [10.1016/S1359-6454\(02\)00505-0](https://doi.org/10.1016/S1359-6454(02)00505-0).
- 50 D. Zöllner, A New Point of View to Determine the Simulation Temperature for the Potts Model Simulation of Grain Growth, *Comput. Mater. Sci.*, 2014, **86**, 99–107, DOI: [10.1016/j.commatsci.2014.01.044](https://doi.org/10.1016/j.commatsci.2014.01.044).
- 51 M. Soucaïl, R. Messina, A. Cosnuau and L. P. Kubin, *Monte Carlo Simulation of Zener Pinning in Two Dimensions*, 1999, vol. 271. <https://www.elsevier.com/locate/msea>.
- 52 W. T. Read and W. Shockley, Dislocation Models of Crystal Grain Boundaries, *Phys. Rev.*, 1950, **78**(3), 275–289, DOI: [10.1103/PhysRev.78.275](https://doi.org/10.1103/PhysRev.78.275).
- 53 A. Paszke, S. Gross, F. Massa, A. Lerer, J. Bradbury, G. Chanan, T. Killeen, Z. Lin, N. Gimelshein, L. Antiga, A. Desmaison, A. Köpf, E. Yang, Z. DeVito, M. Raison, A. Tejani, S. Chilamkurthy, B. Steiner, L. Fang, J. Bai and S. Chintala, *PyTorch: An Imperative Style*, High-Performance Deep Learning Library, 2019.
- 54 S. Kim, C. Jung, H. Kim, K. E. Thomas-Alyea, G. Yoon, B. Kim, M. E. Badding, Z. Song, J. M. Chang, J. Kim, D. Im and K. Kang, The Role of Interlayer Chemistry in Li-Metal Growth through a Garnet-Type Solid Electrolyte, *Adv. Energy Mater.*, 2020, **10**(12), 1903993, DOI: [10.1002/aenm.201903993](https://doi.org/10.1002/aenm.201903993).
- 55 A. D. Pelton, The Au–Li (Gold–Lithium) System, *Bull. Alloy Phase Diagrams*, 1986, **7**(3), 228–231, DOI: [10.1007/BF02868994](https://doi.org/10.1007/BF02868994).
- 56 S. Kotakadi, J. Aspinall, M. Burton, Y. Liang, Y. Aihara and M. Pasta, Impact of Metallic Interlayers at the Lithium–Li<sub>6</sub>PS<sub>5</sub>Cl Solid Electrolyte Interface, *Joule*, 2025, 102175, DOI: [10.1016/j.joule.2025.102175](https://doi.org/10.1016/j.joule.2025.102175).
- 57 M. Hiratani, Effect of a Lithium Alloy Layer Inserted between a Lithium Anode and a Solid Electrolyte, *Solid State Ionics*, 1988, **28–30**, 1406–1410, DOI: [10.1016/0167-2738\(88\)90394-3](https://doi.org/10.1016/0167-2738(88)90394-3).
- 58 J. Sangster and A. D. Pelton, The Bi–Li (Bismuth–Lithium) System, *J. Phase Equilib.*, 1991, **12**(4), 447–450, DOI: [10.1007/BF02645966](https://doi.org/10.1007/BF02645966).
- 59 K. Y. Cho, S. Cho, G. Y. Jung and K. S. Eom, Metal Shields with Crystallographic Discrepancies Incorporated into Integrated Architectures for Stable Lithium Metal Batteries, *Energy Environ. Sci.*, 2024, **17**(9), 3123–3135, DOI: [10.1039/d3ee02372a](https://doi.org/10.1039/d3ee02372a).
- 60 C. V. Thompson, Grain Growth in Thin Films, *Annu. Rev. Mater. Sci.*, 1990, **20**(1), 245–268, DOI: [10.1146/annurev.ms.20.080190.001333](https://doi.org/10.1146/annurev.ms.20.080190.001333).
- 61 P. A. Manohar, M. Ferry and T. Chandra, Five Decades of the Zener Equation, *ISIJ Int.*, 1998, **38**(9), 913–924, DOI: [10.2355/isijinternational.38.913](https://doi.org/10.2355/isijinternational.38.913).
- 62 A. D. Pelton, The Ag–Li (Silver–Lithium) System, *Bull. Alloy Phase Diagrams*, 1986, **7**(3), 223–228, DOI: [10.1007/BF02868993](https://doi.org/10.1007/BF02868993).
- 63 B. Aktekin, L. M. Riegger, S.-K. Otto, T. Fuchs, A. Henss and J. Janek, SEI Growth on Lithium Metal Anodes in Solid-State Batteries Quantified with Coulometric Titration Time Analysis, *Nat. Commun.*, 2023, **14**(1), 6946, DOI: [10.1038/s41467-023-42512-y](https://doi.org/10.1038/s41467-023-42512-y).
- 64 C. D. Alt, N. U. C. B. Müller, L. M. Riegger, B. Aktekin, P. Minnmann, K. Pepller and J. Janek, Quantifying Multiphase SEI Growth in Sulfide Solid Electrolytes, *Joule*, 2024, **8**(10), 2755–2776, DOI: [10.1016/j.joule.2024.07.006](https://doi.org/10.1016/j.joule.2024.07.006).
- 65 J. K. Eckhardt, P. J. Klar, J. Janek and C. Heiliger, Interplay of Dynamic Constriction and Interface Morphology between Reversible Metal Anode and Solid Electrolyte in Solid State Batteries, *ACS Appl. Mater. Interfaces*, 2022, **14**(31), 35545–35554, DOI: [10.1021/acsami.2c07077](https://doi.org/10.1021/acsami.2c07077).

